IEEE Access
Multidisciplinary ⋮ Rapid Review ⋮ Open Access Journal

Received August 30, 2021, accepted September 8, 2021, date of publication September 10, 2021, date of current version October 6, 2021.

Digital Object Identifier 10.1109/ACCESS.2021.3111959

Parasitic High Q-Factor Open-Box Modes With 3-D Printed Dielectric-Filled Metal Waveguides

ATTIQUE DAWOOD AND STEPAN LUCYSZYN, (Fellow, IEEE)
Department of Electrical and Electronic Engineering, Imperial College London, London SW7 2AZ, U.K.

Corresponding author: Stepan Lucyszyn (s.lucyszyn@imperial.ac.uk)

This work was supported in part by the U.K. Space Agency's Centre for Earth Observation Instrumentation (CEOI) under Grant RP10G0435A202.

ABSTRACT High Q-factor open-box mode resonances have been found in the microwave measurements of several 3-D printed dielectric-filled metal-pipe rectangular waveguides (MPRWGs). These parasitic Fabry-Pérot eigenmodes are confined by the conductive walls in the transverse plane of the MPRWG and partially confined by the air-dielectric and dielectric-air boundaries in the longitudinal direction. The excitation of open-box modes was previously speculated to be due to the inhomogeneous and/or anisotropic nature of the 3-D printed dielectric-fillers. This has now been confirmed, by representing the inhomogeneous and anisotropic nature of the woodpile-like dielectric structure (physical realm), with an anisotropic dielectric constant tensor (simulation realm). Analytical and numerical eigenmode solvers, previously used by the authors with MPRWGs, are applied here to parallel-plate waveguides (PPWGs) and circular waveguides (CWGs); identifying all the individual parasitic open-box modes. With the former, its TM_{11} mode exhibits an ultra-high Q-factor of approximately 2,300 at X-band, which is considerably higher than those found with other modes and in other waveguide structures. Finally, a numerical full-wave frequency-domain simulator that employs the dielectric constant tensor is introduced in this paper. This new modeling technique independently confirms that open-box modes are excited in 3-D printed dielectric-filled MPRWG, PPWG and CWG structures. This paper provides the foundations for accurately modeling parasitic resonances associated with inhomogeneities and anisotropy in 3-D printed microwave components; not just the metal-walled waveguide structures considered here, but the methodology could also be extended to generic 3-D printed dielectric waveguides and substrate-based transmission lines.

INDEX TERMS Additive manufacturing, 3-D printing, microwave, dielectric, quality factor, waveguide, resonance, Fabry-Pérot, eigenmode, open-box mode.

I. INTRODUCTION

Over the past decade, 3-D printing of microwave components has gained increasing popularity, due to the availability of affordable 3-D printers that provide a cost-effective solution for prototyping microwave components [1]. This paper will only focus on the X-band (8 to 12 GHz) and Ku-band (12 to 18 GHz) parts of the microwave spectrum. 3-D printed air-filled metal-pipe rectangular waveguides (MPRWGs) were first demonstrated by D'Auria *et al.* in 2015 [2], operating at X-band and W-band (75 to 110 GHz). The following year, a 3-D printed mechanically-tunable X-band MPRWG phase shifter was reported by Gillatt *et al.*, employing a moveable dielectric insert [3]. In 2019, this 3-D printed MPRWG technology was then used to realize a complete steerable Ku-band phased-array antenna subsystem, employing four independent dielectric insert phase shifters [4]. To support these applications, spectroscopic techniques have been developed to accurately characterize the low-loss acrylonitrile butadiene-styrene (ABS) dielectric used in both phase shifters at X-band [5] and more recently at Ku-band [6].

In principle, resonant box modes can exist in any arbitrary 3-D structure that is surrounded by conductive walls. Common examples include rectangular, cylindrical and spherical resonators. Such structures can either be exploited (e.g., engineered to realize filters) or can produce unwanted parasitic effects (e.g., spurious closed-box modes in packaging). In contrast, resonant 'open-box' modes can exist in any arbitrary dielectric-filled 3-D structure that is partially

The associate editor coordinating the review of this manuscript and approving it for publication was Feng Lin.

surrounded by conductive walls. With a MPRWG, the open-box modes are confined by the conductive walls in the transverse plane and partially confined by the air-dielectric and dielectric-air boundaries in the longitudinal direction.

When measuring a dielectric-filled MPRWG between a pair of traditional air-filled MPRWGs, associated with the vector network analyzer's (VNA's) test-set heads, the driven Fabry-Pérot resonance will be excited. For the MPRWG, the dominant transverse electric (TE) mode of propagation is the TE_{10} mode. In addition to the expected spectral dips in $|S_{11}|$ and peaks in $|S_{21}|$, associated with the driven Fabry-Pérot resonance, the measured scattering (S-)parameters show anomalous notches in $|S_{11}|$ and $|S_{21}|$ at fixed frequencies. The authors previously referred to these resonances as 'open-box' modes [5], [6]; they may also be referred to as 'parasitic Fabry-Pérot eigenmodes'. Excitation of parasitic open-box modes in 3-D printed woodpile-like cuboids were previously attributed to their inhomogeneous and/or anisotropic nature [5], [6].

High Q-factor open-box mode resonances have been found in microwave measurements of several 3-D printed dielectric-filled MPRWGs [5]–[9]. With conventional *a priori* frequency-domain modeling, these parasitic Fabry-Pérot eigenmodes cannot be predicted using analytical technique and may be difficult to predict using 'to-scale' numerical full-wave electromagnetic simulations; although an analytical or numerical eigenmode solver can be used.

In 2015, using an ultraviolet (UV)-cured ink-jet type 3-D printer, the U.S. Airforce Institute of Technology investigated both solid (homogenous) and periodic (inhomogeneous) polytetrafluoroethylene (PTFE) cuboids; the latter introduces periodic airgaps (rectangular inclusions) to create a biaxial anisotropic dielectric constant [7]. With this biaxial anisotropic material, X-band measurements of a dielectric-filled WR-90 MPRWG clearly show an open-box mode resonance at 10.4 GHz (not mentioned in their report). With their quoted value of effective dielectric constant of 2.1, using our analytical eigenmode solver, we found this to be the TE_{201} open-box mode predicted at 10.45 GHz. Interestingly, using rectangular-to-square waveguide transitions, cubic sample measurements did not appear to show any open-box mode resonances [7].

Isakov *et al.* [8] demonstrated 3-D printed metamaterials by deliberately introducing inhomogeneity and anisotropy; either ABS or polypropylene (PP) was used for the low dielectric constant regions, while a mixed inorganic ceramic powder ($BaTiO_3$) and polymer (ABS) composite was used for high dielectric constant regions. Both striped and checkered cuboids (2 mm thick samples) were 3-D printed and inserted into Ku-band MPRWGs. With eight interleaving horizonal strips (having alternating dielectric constant values of 2.6 and 7.0), using the *COMSOL Multiphysics*® frequency-domain simulator, resonances at 15.19 GHz and 19.54 GHz are observed. The Oxford group attribute these resonances with the "*first* TE_{11} *mode and second* TE_{12} *mode of the Mie-resonances (magnetic and electric, respectively)*". Ku-band measurements revealed a very weak resonance at 12.7 GHz and a strong resonance at 15.9 GHz. However, by observing their simulated field plots [8] and using both our analytical and numerical eigenmode solvers, we found that these resonances are actually TE_{111} and transverse magnetic (TM) TM_{111} open-box modes. Moreover, the weaker resonance at 12.7 GHz, only observed in measurements, can be attributed to the TE_{201} open-box mode. The subtle difference in mode interpretation is that Mie resonances are associated with unbound objects, while open-box modes are partially constrained by conducting sidewalls.

Yang *et al.* [9] reported the characterization of 3-D printed polylactic acid (PLA) cuboid samples at X-band. Dielectric-filled MPRWG measurements, having different filler lengths, indicate the presence of parasitic open-box mode resonances (not mentioned in their paper).

Parasitic Fabry-Pérot eigenmodes were previously identified and characterized in MPRWGs, having 3-D printed ABS dielectric fillers; at X-band by Sun *et al.* [5] and Ku-band by Márquez-Segura *et al.* [6]. In both cases, the ABS dielectric fillers were 3-D printed using fused deposition modeling (FDM). Interestingly, open-box modes were not found with conductive PLA cuboids, as they are heavily damped by the presence of carbon black powder [6].

These open-box modes were investigated using both analytical and numerical eigenmode solvers, but our previous analyses were restricted to just MPRWGs. Moreover, we used an irregular coarse tetrahedral meshing scheme within *COMSOL Multiphysics*® frequency-domain simulator to excite the open-box modes; representing an artificial form of inhomogeneity and/or anisotropy (to demonstrate proof of concept). However, this coarse meshing scheme (simulation realm) is not a reliable way of accurately modeling an actual waveguide structure (physical realm).

In order to investigate the propagating and non-propagating modes associated with transmission lines and guided-wave structures, various analytical and numerical methods can be used. With the former, the *variational* method is very accurate above and below the cut-off frequency; while the more simplified textbook *power-loss* approximations can also be used for frequency-domain simulations above the cut-off frequency to good effect [5]. Moreover, analytical equations can be derived to give complex eigenfrequencies. With the latter, finite-element methods can be employed with both numerical full-wave frequency-domain simulators and eigenmode solvers. With numerical frequency-domain simulators, non-propagating modes can only be inferred from its spectral response; while eigenmode solvers give direct solutions as complex eigenfrequencies, even if the dielectric is represented as being homogenous and isotropic [5]. The *COMSOL Multiphysics*® RF Module has both a finite-element based numerical full-wave frequency-domain simulator and eigenmode solver [10]; the former provides a complex steady-state response for each swept frequency point, while the latter gives the complex eigenfrequencies associated with all possible eigenmodes for the structure.

In this paper, we introduce a reliable method for accurately predicting the excitation of open-box modes in MPRWGs by introducing controlled inhomogeneity and anisotropy in the dielectric filler, using the *COMSOL Multiphysics*® frequency-domain simulator. In addition, the excitation of open-box modes in dielectric-filled parallel-plate waveguides (PPWGs) and circular waveguides (CWGs) are investigated. Finally, we demonstrate the accuracy of our predictions using both analytical and numerical eigenmode solvers.

Our previously derived analytical expressions for MPRWGs (Appendix B in [5]) have been adapted to also include PPWGs and CWGs. These are then used to verify the numerical results from *COMSOL Multiphysics*®. The generic analytical derivations, given in the Appendix, provide continuity between the different waveguide structures and completeness by including both TE and TM modes. Moreover, perfect electric conductor (PEC) walls are assumed throughout, to eliminate uncertainty in the extracted mode quality (Q-)factor, associated with the simulated boundary conditions used to approximate real metal walls. Also, throughout this paper, our analytical methods adopt the simplified textbook *power-loss* approximations.

II. PROPAGATION CONSTANT IN GUIDED MEDIA

In any medium (unbound or guided), the generic complex propagation constant is given by [5],

$$\gamma = \alpha + j\beta \equiv jk \tag{1}$$

where, α is the attenuation constant, β is the phase constant and k is the complex angular wavenumber.

With a waveguide, a cut-off propagation constant can be defined as $\gamma_c = jk_c$, where $k_c \equiv \beta_c$ is the cut-off angular wavenumber (real value); $\beta_c = \omega_c/v_p$ is the phase constant associated with angular cut-off frequency $\omega_c = 2\pi f_c$ and phase velocity $v_p = c/Re\{\tilde{n}\}$ for a dielectric-filled waveguide, $f_c = k_c c/2\pi Re\{\tilde{n}\}$ is the cut-off frequency; $c = 1/\sqrt{\mu_0\varepsilon_0}$ is the speed of light in free space, where μ_0 and ε_0 are the permeability and permittivity of free space, respectively; and $\tilde{n}$ is the complex refractive index for an unbounded dielectric medium.

For a waveguide having PEC walls, operating in the TE_{mn} or TM_{mn} mode, with propagation along the longitudinal z-direction, the general textbook expression for guided-wave propagation constant γ_g is,

$$\gamma_g^2 = \gamma_{ud}^2 - \gamma_{cmn}^2 \equiv \gamma_{mn}^2 \tag{2}$$

All variables have their usual meaning, where the subscripts m and n are the mode indices denoting the number of half-wavelength variations of the fields in the transverse plane; γ_{cmn} is the cut-off propagation constant in the waveguide; γ_{ud} is the propagation constant in an unbound dielectric medium with $\gamma_{ud} = jk_{ud} = j\omega\sqrt{\tilde{\mu}_{eff}\tilde{\varepsilon}_{eff}} = \omega\sqrt{\tilde{\mu}_{reff}\tilde{\varepsilon}_{reff}}/c$, where $\omega = 2\pi f$ is the angular frequency, f is the frequency; $\tilde{\mu}_{reff} = \mu'_{reff} - j\mu''_{reff}$ (the dielectric is assumed non-magnetic in this paper) and $\tilde{\varepsilon}_{reff} = \varepsilon'_{reff} - j\varepsilon''_{reff}$ are the effective complex relative permeability and permittivity, respectively, for the unbound dielectric; loss tangent is defined as $tan\delta = Im\{\tilde{n}^2\}/Re\{\tilde{n}^2\}$, where $\tilde{n} = \sqrt{\tilde{\mu}_{reff}\tilde{\varepsilon}_{reff}}$; ε'_{reff} and $tan\delta_e = \varepsilon''_{reff}/\varepsilon'_{reff}\big|_{\mu''_{reff}=0}$ are the dielectric constant and loss tangent of the unbound dielectric, respectively, since $tan\delta = tan\delta_e$ with $\mu''_{reff} = 0$.

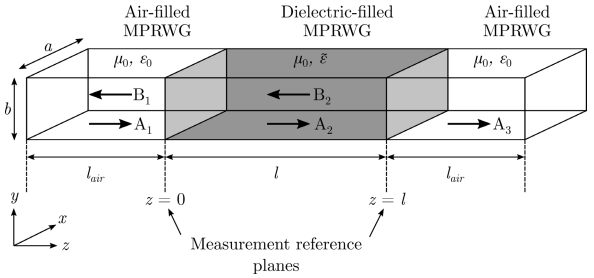

FIGURE 1. Illustration of an ideal dielectric-filled metal-pipe rectangular waveguide having internal dimensions *a* and *b*. The length of the dielectric cuboid and air-filled sections are *l* and l_{air}, respectively. In any section, *A*s and *B*s are the incident and reflected waves, respectively. This figure is redrawn from Sun *et al.* [5].

III. METAL-PIPE RECTANGULAR WAVEGUIDES

A. BACKGROUND

With both the TE_{mn} and TM_{mn} modes for a MPRWG, the textbook cut-off propagation constant is,

$$\gamma_{cmn} = jk_{cmn} = j\sqrt{\left(\frac{m\pi}{a}\right)^2 + \left(\frac{n\pi}{b}\right)^2} \tag{3}$$

and,

$$k_{cmn} = \beta_{cmn} = \omega_{cmn}/v_p \tag{4}$$

were, m and n correspond to the mode numbers in the horizontal x- and vertical y-directions in the transverse plane, respectively; $k_{cmn} = \sqrt{(m\pi/a)^2 + (n\pi/b)^2}$ is the cut-off angular wavenumber for either an air- or dielectric-filled waveguide; $\omega_{cmn} = 2\pi f_{cmn}$ and $f_{cmn} = k_{cmn}v_p/2\pi$ are the cut-off angular frequency and cut-off frequency, respectively.

Consider the MPRWG structure illustrated in Fig. 1, where a TE_{mn} or TM_{mn} mode is incident on the dielectric-filled section. For a WR-90/WR-62 waveguide operating at X-/Ku-band, in the dominant TE_{10} mode, the ideal internal cross-sectional dimensions are $a = 22.860/15.799$ mm and $b = 10.160/7.899$ mm; while the length of the dielectric-filled section is $l = 9.626/6.676$ mm [5]/[6].

An FDM 3-D printed sample is generally composed of dielectric layers, deposited layer-by-layer; even with a 100% infill printer setting, unintentional airgaps can effectively create a woodpile structure [5], [6]. Figure 2 illustrates layer-by-layer FDM 3-D printing of a dielectric cuboid, showing alternate layers having a 90° angular offset in the printed strips and adjacent air gaps. As a result, the FDM 3-D printed MPRWG cuboid dielectric filler should be considered inhomogeneous and anisotropic in nature.

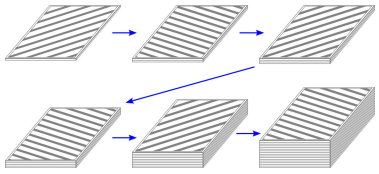

FIGURE 2. Layer-by-layer illustration of an FDM 3-D printed cuboid showing alternating 90° offsets for the strips and air gaps (black lines in the *x-y* plane of the build surface) creating a woodpile-like structure.

B. EXCITATION OF OPEN-BOX MODE RESONANCES WITH FREQUENCY-DOMAIN SIMULATOR

We previously speculated (without demonstrable proof) that the excitation of open-box modes is due to the inhomogeneous and/or anisotropic nature of our dielectric filler within MPRWGs [5], [6]. To-scale numerical electromagnetic modeling of our 3-D woodpile-like structure was not possible, given the limited computational resources available, as extremely fine meshing is required for the very small spatial features [5]. Up-scaling the spatial features or introducing minor defects to the cuboid geometry could not excite parasitic open-box modes associated with our woodpile-like structure. However, we were able to observe open-box mode resonances when an overly coarse meshing scheme was applied with purely homogenous and isotropic dielectric samples; using the *COMSOL Multiphysics*® frequency-domain simulator. With a finer meshing scheme, the open-box modes could not be observed.

A coarse meshing scheme can only give a qualitative prediction for the spectral locations of open-box modes. Moreover, this approach does not appear to work with other types of waveguides (e.g., parallel-plate and circular). For these reasons, an improved modeling scheme for predicting the excitation of open-box modes in dielectric-filled waveguides is needed.

The following method exploits the real part of the complex effective relative permittivity (dielectric constant) tensor $\left[\varepsilon'_{reff}\right]$ within the *COMSOL Multiphysics*® frequency-domain simulator. This tensor represents an anisotropy for the dielectric-filler within any waveguide structure; allowing accurate predictions to be made for the parasitic open-box modes found with conventional microwave VNA measurements.

The generalized dielectric constant tensor can be expressed in (5), as shown at the bottom of the next page, where, ε'_{reffx}, ε'_{reffy}, ε'_{reffz} are bulk dielectric constant values in the respective x, y, z directions, with ε'_{reffx}, ε'_{reffy}, $\varepsilon'_{reffz} = \varepsilon'_{reff}$ given an isotropic dielectric; $c_{uv}\,(u, v \in \{x, y, z\})$ are scalar coefficients that represent the level of coupling between different field components due to anisotropy, with $c_{uv} = 0$ given an isotropic dielectric; and $f_{uv}\,(x, y, z)$ are scalar functions that represent spatial inhomogeneity, with $f_{uv} = 0$ (or any constant value) given a homogenous dielectric.

With FDM 3-D printed cuboids having a 100% infill printer setting, we previously demonstrated anisotropy for conducive PLA cuboids [6]. It was shown that the extracted bulk dielectric properties are different when TE_{10} mode propagation within the dielectric-filled MPRWG is along build layers and against build layers [6]; for example, with the latter, ε'_{reffx}, $\varepsilon'_{reffy} \neq \varepsilon'_{reffz}$. However, for simplicity, when comparing numerical simulations with analytical modeling, ε'_{reffx}, ε'_{reffy}, $\varepsilon'_{reffz} = \varepsilon'_{reff}$. Moreover, since the dielectric-filled waveguide is both passive and reciprocal, to preserve its symmetrical S-parameter matrix, a symmetric dielectric constant tensor must be employed (with $uv = vu$). Note that a truly isotropic dielectric must satisfy all the following conditions: (i) $\varepsilon'_{reffx}, \varepsilon'_{reffy}, \varepsilon'_{reffz} = \varepsilon'_{reff}$; (ii) $c_{uv} = 0$; and (iii) $f_{uv} = 0$ (or any constant value).

To ensure an effective bulk value for ε'_{reff}, f_{uv} should be chosen to have a zero mean spatial value over the x, y, z directions of the dielectric. For simplicity, f_{uv} is chosen to have the following linear spatial variation,

$$f_{uv} = \pm\Delta^{\%}_{\varepsilon'_{reffx}} \frac{(x - a/2)}{a} \pm \Delta^{\%}_{\varepsilon'_{reffy}} \frac{(y - b/2)}{b} \pm \Delta^{\%}_{\varepsilon'_{reffz}} \frac{(z - l/2)}{l} \tag{6}$$

where, $\Delta^{\%}_{\varepsilon'_{reffx}}$, $\Delta^{\%}_{\varepsilon'_{reffy}}$ and $\Delta^{\%}_{\varepsilon'_{reffz}}$ represent the maximum normalized percentage variation in ε'_{reff} along x, y and z directions, respectively. For example, a 5% variation (corresponding to a ±2.5% change) in dielectric constant along the x-direction has,

$$\Delta^{\%}_{\varepsilon'_{reffx}} = \frac{5}{100} = 0.05 \tag{7}$$

For simplicity, and throughout this paper, $\Delta^{\%}_{\varepsilon'_{reffx}} = \Delta^{\%}_{\varepsilon'_{reffy}} = \Delta^{\%}_{\varepsilon'_{reffz}} = \Delta^{\%}_{\varepsilon'_{reff}}$ can be chosen as a single parameter for the variation in ε'_{reff} along all axial directions. Moreover, with a symmetrical network, $c_{uv} = c_{vu}$ and $f_{uv} = f_{vu}$.

Within *COMSOL Multiphysics*®, using (5), the signs for the terms in (6) are arbitrarily chosen for our simulated MPRWG, as follows,

$$f_{xx} = f_{xy} = f_{yx} = \Delta^{\%}_{\varepsilon'_{reff}} \left(-\frac{(x - a/2)}{a} + \frac{(y - b/2)}{b} + \frac{(z - l/2)}{l} \right) \tag{8}$$

$$f_{yy} = f_{yz} = f_{zy} = \Delta^{\%}_{\varepsilon'_{reff}} \left(\frac{(x - a/2)}{a} - \frac{(y - b/2)}{b} + \frac{(z - l/2)}{l} \right) \tag{9}$$

$$f_{zz} = f_{zx} = f_{xz} = \Delta^{\%}_{\varepsilon'_{reff}} \left(\frac{(x - a/2)}{a} + \frac{(y - b/2)}{b} - \frac{(z - l/2)}{l} \right) \tag{10}$$

with all the scalar coefficients $c_{uv} = 1$ and a 2% variation of the dielectric constant in all axial directions. The choice of f_{uv} assumes the origin $(x, y, z = 0)$ is located at one of the corners of the dielectric filler.

C. SIMULATED SPECTRAL RESPONSES

Waveguides usually operate in a single mode. However, with mode conversion, normal ports in electromagnetic simulation software treat hybrid modes as single modes. The driven excitation mode (TE_{10} in this case) must be chosen at the input port within the *COMSOL Multiphysics*® frequency-domain simulator. The S-parameters are calculated at each port from the driven excitation mode and a specified mode (which may be different to the driven mode, but not in this case); using their transverse field profiles (parallel to the port surfaces). Therefore, before simulations begin, the specified mode being analysed must be defined at each port. By default, within *COMSOL Multiphysics*®, the simulation space is terminated by a port boundary condition, which absorbs only the specified mode at that port; reflecting all other modes.

Propagating (i.e., driven and spurious) and non-propagating spurious (i.e., not driven or specified) modes can be excited within a waveguide having an embedded dielectric-filled section, due to inhomogeneity and/or anisotropy; these unmatched modes will be reflected from the ports – back into the simulation space. Indeed, using our chosen dielectric constant tensor, with (8)-(10), it was found that the ports reflected all non-TE_{10} modes. As a result, the complete structure (which includes the two air-filled waveguide sections) acts as a closed-box resonator containing all spurious (including both closed- and open-box) modes. The open-box modes are excited within the central dielectric-filled waveguide section with decaying evanescent fields in the air-filled sections.

For multimode conditions, *COMSOL Multiphysics*® has the option of defining theoretical *'slit'* ports, which mathematically allow all propagating modes to pass through without reflections or absorption. Therefore, a perfectly matched layer (PML) is also needed behind the slit port, to avoid any subsequent reflections, as illustrated in Fig. 3. These slit ports have no interaction with the waveguide fields, but can be used to excite or record fields (e.g., to calculate S-parameters) like normal ports.

All natural resonances are characterized by their complex eigenfrequency [11],

$$\tilde{f}_0 = f_0' + jf_0'' \tag{11}$$

where, f_0' is the damped (undriven) resonance frequency and $2\pi f_0''$ is the Napier frequency (or field (amplitude) decay rate or loss rate). Conventional VNA measurements of MPRWGs, having FDM 3-D printed dielectric filler cuboids, can reveal unexpected spectral notches in the S-parameters. With the VNA's steady-state frequency-domain responses,

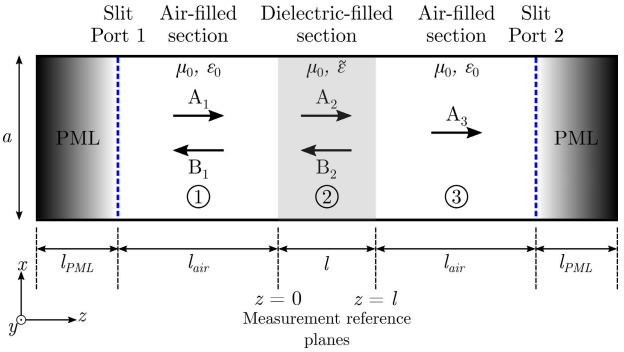

FIGURE 3. Illustration of the simulated metal-pipe rectangular waveguide showing the dielectric-filled, air-filled and perfectly matched layer (PML) sections. Two slit ports (shown as blue dashed lines) are defined at the ends of the air-filled sections with excitation at Port 1.

spectral notches represent the undamped (driven) resonance frequency $f_0 = \left|\tilde{f}_0\right|$. For an ideal resonator without losses, $f_0'' = 0$ and $f_0 = \tilde{f}_0 = f_0'$. Both the respective damped and undamped unloaded Q-factors for a resonance can be given as [11],

$$Q_u(f_0') = \frac{f_0'}{2f_0''} \tag{12}$$

and

$$Q_u(f_0) = \frac{f_0}{2f_0''} = \sqrt{0.25 + Q_u^2(f_0')} \tag{13}$$

With reference to Fig. 1, the dominant TE_{10} mode calibrated measurement reference planes are physically located at the air-dielectric ($z = 0$) and dielectric-air ($z = l$) boundaries within the MPRWG. However, the simulation reference planes are located at the slit ports. Therefore, the simulated S-parameters for the TE_{10} mode must be de-embedded (shifting the measurement reference planes to the dielectric filler), to mathematically remove the air-filled sections. This can be achieved by simply multiplying S_{11} and S_{21} with $e^{+2\gamma_{mn}l_{air}}$; the brass-walled air-filled waveguide sections can be treated as lossless in practice. The lengths of the air-filled and PML sections are $l_{air} = l_{PML} = 2l = 19.252$ mm, used for the numerical frequency-domain simulations at X-band; the dielectric filler has $\varepsilon'_{reff②} = 2.3284$ and $tan\delta_{e②} = 19.1480 \times 10^{-4}$, corresponding to X-band values for ABS Sample #1 from Table 1 in [5].

Previously [5], the analytical S-parameter modeling and all numerical simulations used brass conductors (to model the physical realm), while PEC was used for the analytical eigenmode solver. Here, PEC is used in all simulations,

$$\left[\varepsilon'_{reff}\right] = \begin{bmatrix} \varepsilon'_{reffx}\left(1 + f_{xx}(x,y,z)\right) & c_{xy}f_{xy}(x,y,z) & c_{xz}f_{xz}(x,y,z) \\ c_{yx}f_{yx}(x,y,z) & \varepsilon'_{reffy}\left(1 + f_{yy}(x,y,z)\right) & c_{yz}f_{yz}(x,y,z) \\ c_{zx}f_{zx}(x,y,z) & c_{zy}f_{zy}(x,y,z) & \varepsilon'_{reffz}\left(1 + f_{zz}(x,y,z)\right) \end{bmatrix} \tag{5}$$

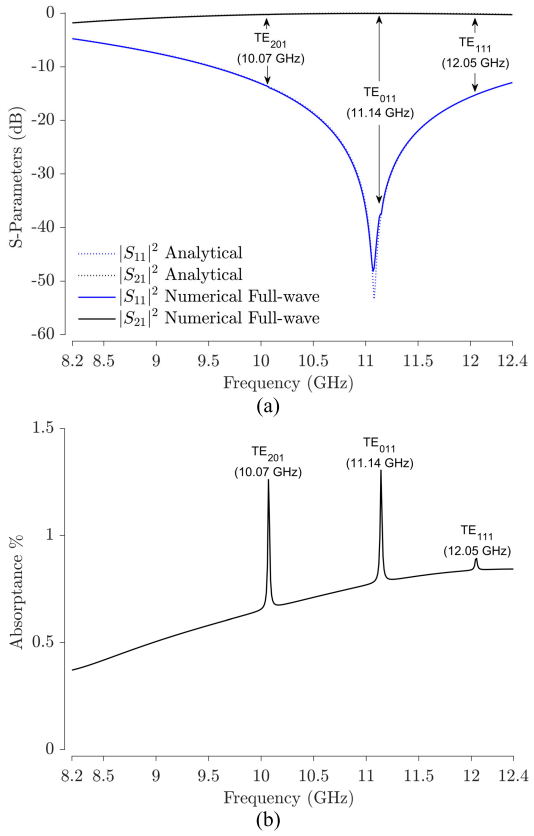

FIGURE 4. Simulated ABS-filled and PEC-walled X-band metal-pipe rectangular waveguide spectral responses: (a) $|S_{11}|^2$ and $|S_{21}|^2$; and (b) corresponding absorptance from numerical full-wave simulations.

to give a better Q-factor match between analytical and numerical eigenmode solver results. Moreover, finer meshing is introduced for the numerical frequency-domain simulator, to further increase accuracy. Finally, we employ the dielectric constant tensor and the use of slit ports with PML waveguide sections.

For the X-band MPRWG operating in the dominant TE_{10} mode, the simulated $|S_{11}|^2$ and $|S_{21}|^2$ frequency responses are given in Fig. 4(a). The solid lines in Fig. 4(a) correspond to numerical frequency-domain simulations (using *COMSOL Multiphysics*®), while dotted lines correspond to our analytical textbook S-parameter modeling, using (A23) and (A26)-(A30) in the Appendix; both clearly predicting the driven Fabry-Pérot resonance at 11.14 GHz. Figure 4(b) shows the absorptance $\mathcal{A}$ calculated using [5],

$$\mathcal{A} = 1 - |S_{11}|^2 - |S_{21}|^2 \tag{14}$$

Note that (14) is only valid for passive, symmetrical and reciprocal two-port networks. The absorptance spectrum, given in Fig. 4(b), clearly shows parasitic TE_{201}, TE_{011} and TE_{111} open-box mode resonances at $f_{201}^{TE} = 10.07$ GHz, $f_{011}^{TE} = 11.14$ GHz and $f_{111}^{TE} = 12.05$ GHz, respectively. The spectral location of these open-box modes can also be determined from local minima (dips) in $|S_{21}|^2$; not clearly seen in Fig. 4(a).

TABLE 1. Open-box mode resonance frequencies (and associated mode Q-factors) spectroscopically measured (brass-walled) and predicted (PEC) using analytical and numerical eigenmode solvers and numerical frequency-domain simulator for X-band. Measured values are for Sample #1 from Sun *et al.* [5].

Open-box Mode		TE_{101}	TE_{201}	TE_{011}	TE_{111}
$\lvert\tilde{f}_{mnp}\rvert$ [GHz]	Measured	Below cut-off	10.115	11.115	12.065
$\tilde{f}_{mnp}$ ($\lvert\tilde{f}_{mnp}\rvert$) [$Q_u(f_{mnp})$]	Analytical Eigenmode	5.6065+ j0.0036 (5.6065) [784]	10.0732+ j0.0084 (10.0732) [600]	11.1431+ j0.0095 (11.1431) [585]	12.0450+ j0.0105 (12.0450) [576]
	Numerical Eigenmode	5.6064+ j0.0036 (5.6064) [784]	10.0729+ j0.0084 (10.0729) [600]	11.1428+ j0.0095 (11.1428) [585]	12.0447+ j0.0105 (12.0447) [576]
	Numerical Full-wave	Below cut-off	(10.07)	(11.14)	(12.05)

Using our analytical eigenmode solver, (A35)-(A36) in the Appendix, the dominant TE_{101} open-box mode (loosely related to the driven Fabry-Pérot resonance, in terms of field patterns) was predicted to exist at $f_{101}^{TE} = 5.6065$ GHz and 5.6229 GHz for Samples #1 and #2, respectively, in [5]. These are below the $f_c^{TE\,10} = 6.5571$ GHz cut-off frequency for an air-filled MPRWG and, therefore, outside the intended frequency range of operation for the WR-90 waveguide [5]. The lowest-order TM mode, TM_{111}, has an eigenfrequency of $f_{111}^{TM} = 12.8765$ GHz, which is just above our frequency range of interest.

As seen in Table 1, unlike the previous numerical eigenmode solver Q-factor predictions [5], the new results from our analytical (using (A35) and (A36) in the Appendix) and numerical eigenmode solvers are almost identical. Moreover, the X-band numerical full-wave frequency-domain predictions for the undamped resonance frequencies are within 0.01 GHz of those from both the analytical and numerical eigenmode solvers; and within 0.1 GHz when compared to practical measurements (validating our simulations) [5].

Simulations were repeated for 3-D printed ABS at Ku-band. Here, the lengths of the air-filled and PML sections are $l_{air} = l_{PML} = 2l = 13.352$ mm, used for the numerical frequency-domain simulations at Ku-band; the band-average extracted values for dielectric constant and loss tangent are $\varepsilon'_{reff\,②} = 2.3725$ and $tan\delta_{e\,②} = 16 \times 10^{-4}$, respectively [6]. The S-parameters and absorptance spectra are given in Fig. 5, showing the excitation of parasitic TE_{011}-TE_{201}(coupled), TE_{111} and TM_{111} open-box modes.

The results are summarized in Table 2. Both eigenmode solvers predict the TE_{101} open box-mode below the $f_c^{TE\,10} = 9.4877$ GHz cut-off frequency for an air-filled MPRWG and, therefore, outside the intended frequency range of operation for the WR-62 waveguide [6].

By coincidence, with both analytical and numerical eigenmode solvers, the TE_{011} and TE_{201} open-box modes have the same eigenfrequency, with a predicted undamped resonance frequency of $f_{011}^{TE} = f_{201}^{TE} = 14.449$ GHz. However, with the numerical frequency-domain simulator, these modes appear at both 14.44 and 14.46 GHz; band-splitting due to over-coupling of the TE_{011} and TE_{201} modes can be inferred.

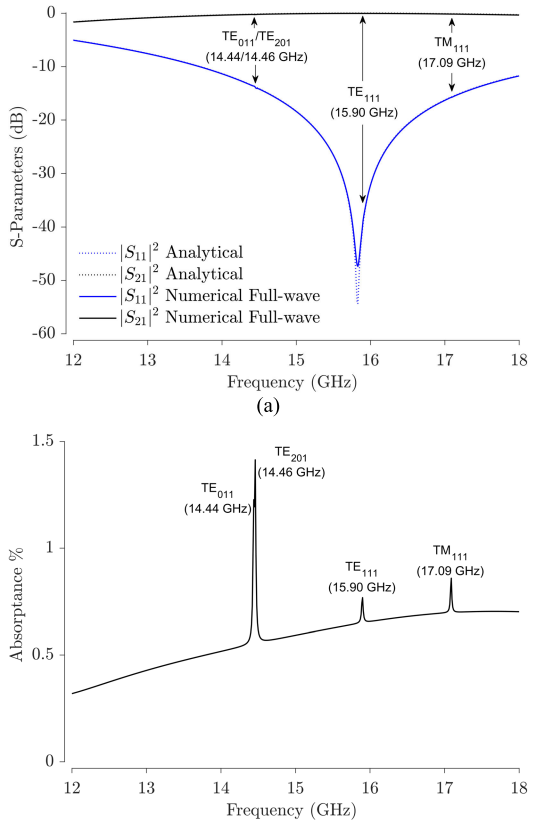

FIGURE 5. Simulated ABS-filled and PEC-walled Ku-band metal-pipe rectangular waveguide spectral responses: (a) $|S_{11}|^2$ and $|S_{21}|^2$; and (b) corresponding absorptance from numerical full-wave simulations.

TABLE 2. Open-box mode resonance frequencies (and associated mode Q-factors) spectroscopically measured (brass-walled) and predicted (PEC) using analytical and numerical eigenmode solvers and numerical frequency-domain simulator for Ku-band. Measured values are for the sample from Márquez-Segura *et al.* [6].

Open-box Mode		TE_{101}	TE_{011}/TE_{201}	TE_{111}	TM_{111}
$\lvert\tilde{f}_{mnp}\rvert$ [GHz]	Measured	Below cut-off	14.25	15.75	16.90
$\tilde{f}_{mnp}$ ($\lvert\tilde{f}_{mnp}\rvert$) [$Q_u(f_{mnp})$]	Analytical Eigenmode	8.0570+ *j*0.0044 (8.0570) [924]	14.4489+ *j*0.0101 (14.4489) [715]	15.8963+ *j*0.0114 (15.8963) [698]	17.0880+ *j*0.0094 (17.0880) [910]
	Numerical Eigenmode	8.0567+ *j*0.0044 (8.0567) [924]	14.4493+ *j*0.0101 (14.4493) [715]	15.8959+ *j*0.0114 (15.8959) [698]	17.0875+ *j*0.0094 (17.0875) [910]
	Numerical Full-wave	Below cut-off	(14.44/14.46)	(15.90)	(17.09)

The Ku-band numerical full-wave frequency-domain predictions for the undamped resonance frequencies are within 0.02 GHz of those from both the analytical and numerical eigenmode solvers; and within approximately 0.2 GHz when compared to practical measurements (once again validating our simulations) [6].

D. IDENTIFYING OPEN-BOX MODE RESONANCES FROM FIELD PLOTS

A numerical eigenmode solver with fine meshing can also be used to create and study the 3-D field plots associated with the parasitic open-box mode resonances. Here, the two air-filled waveguide sections have been increased in length from $l_{air} = 2l$ (used in the numerical frequency domain simulator) to $l_{air} = 11.5l$ (used in the numerical eigenmode solver), allowing the evanescent fields of the open-box modes below cut-off to sufficiently decay outside the dielectric cuboid [5]. Also, the extreme ends of the air-filled sections are terminated with absorbing 'second-order scattering boundary' surfaces, since a PML boundary has a significant spatial volume that has a large computational overhead [5], [10]. Figures 6 to 9 show E-field plots for the parasitic open-box TE mode resonances at X-band [5] and Fig. 10 for the additional TM mode at Ku-band. At X-band, Sun *et al.* [5] found that the parasitic TE_{101}, TE_{011}, TE_{201}, and TE_{111} open-box modes all have even longitudinal symmetry about the center of the sample. Similar field patterns will be found with the open-box modes at Ku-band [6] with the addition of the TM_{111} mode, having odd longitudinal symmetry.

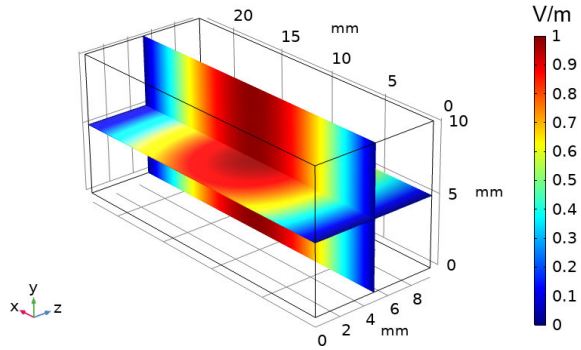

FIGURE 6. Numerically simulated E_x-field plot for the even TE_{101} open-box mode at $f_{101}^{TE} = 5.6064$ GHz for X-band.

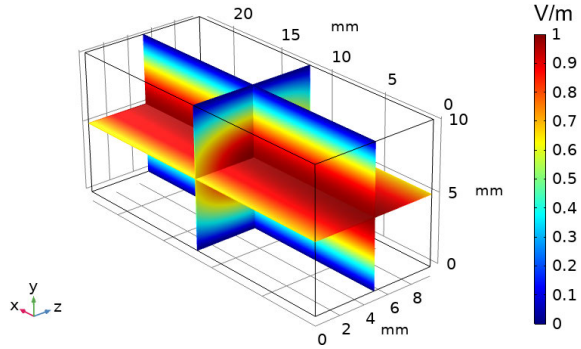

FIGURE 7. Numerically simulated E_x-field plot for the even TE_{011} open-box mode at $f_{011}^{TE} = 11.1428$ GHz for X-band.

IV. PARALLEL-PLATE WAVEGUIDES

A. BACKGROUND

Consider the vertical PEC-walled PPWG shown in Fig. 11, where the structure is assumed to be infinite in the *y*-direction. The length of the dielectric-filled section (②) is l and the air-filled sections (① and ③) have length l_{air}. Following the approach in Section IIIA, assume a TE_m or TM_m mode is incident on the dielectric-filled section.

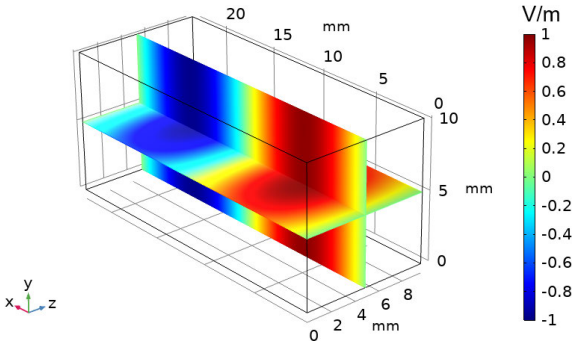

FIGURE 8. Numerically simulated E_y-field plot for the even TE_{201} open-box mode at $f_{201}^{TE} = 10.0729$ GHz for X-band.

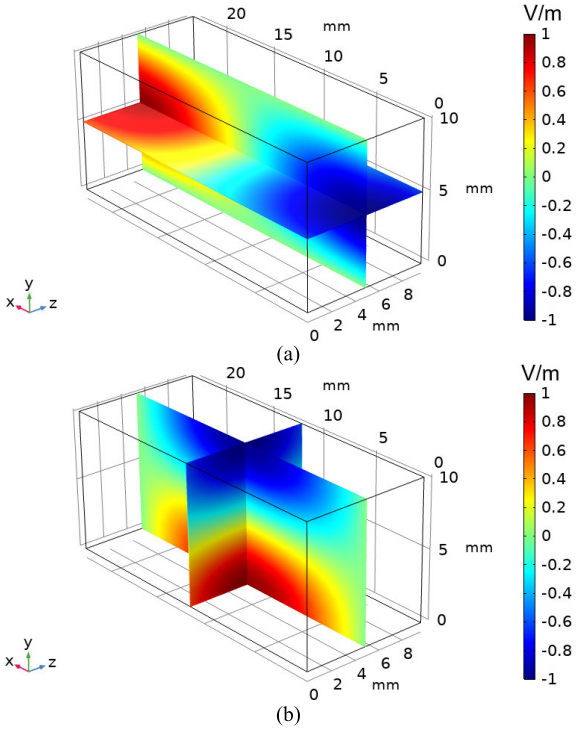

FIGURE 9. Numerically simulated field plots for the even TE_{111} open-box mode at $f_{111}^{TE} = 12.0447$ GHz: (a) E_x-field; and (b) E_y-field for X-band.

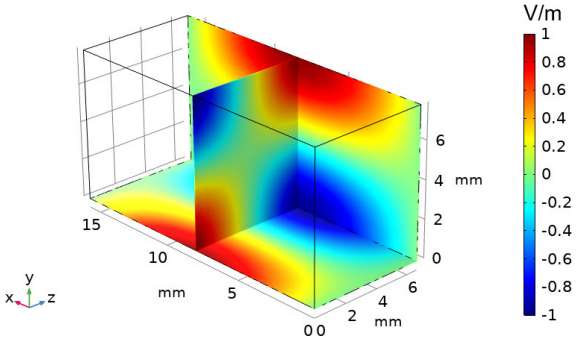

FIGURE 10. Numerically simulated E_y-field plot for the odd TM_{111} open-box mode at $f_{111}^{TM} = 17.0875$ GHz for Ku-band.

With reference to the Appendix, the cut-off propagation constant is now $\gamma_{cm} = jk_{cm} = jm\pi/a$ for air-filled sections, with a representing the internal wall separation distance.

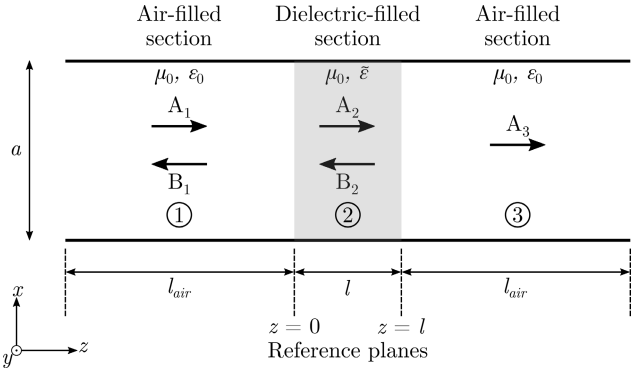

FIGURE 11. Plan view illustration of a vertical PEC-walled dielectric-filled 2-D parallel-plate waveguide having internal wall separation a.

The characteristic matrix equation for TE_m modes is effectively the same as (A12) for TE_{mn} modes with the MPRWG, but without the mode index n in the amplitude coefficients and propagation constant (i.e., $A_{mn} \rightarrow A_m$, $B_{mn} \rightarrow B_m$ and $\gamma_{mn} \rightarrow \gamma_m$). Therefore, the amplitude coefficients correspond to those in (A23)-(A26); the generalized coefficients ζ and ς correspond to (A27) and (A28), respectively; and the S-parameters S_{11} and S_{21} to (A29) and (A30), respectively. In a similar way to that undertaken for the MPRWG, the associated even and odd modes can be obtained by numerically solving the analytical transcendental equations in (A35) and (A36), respectively, for the complex eigenfrequencies.

B. EXCITATION OF OPEN-BOX MODE RESONANCES WITH FREQUENCY-DOMAIN SIMULATOR

Following the approach outlined in Section IIIB, for the excitation of open-box modes using an anisotropic dielectric constant tensor, a 2-D PPWG was simulated using the *COMSOL Multiphysics*® frequency-domain simulator.

Within *COMSOL Multiphysics*®, using (5), the signs for the terms in (6) are arbitrarily chosen for our simulated PPWG, as follows,

$$f_{xx} = \Delta^{\%}_{\varepsilon'_{reff}} \left(-\frac{(x - a/2)}{a} + \frac{(z - l/2)}{l} \right) \tag{15}$$

$$f_{yy} = \Delta^{\%}_{\varepsilon'_{reff}} \left(\frac{(x - a/2)}{a} - \frac{(z - l/2)}{l} \right) \tag{16}$$

$$f_{zz} = f_{xy} = f_{yx} = f_{xz} = f_{zx} = f_{yz} = f_{zy} = \Delta^{\%}_{\varepsilon'_{reff}} \left(\frac{(x - a/2)}{a} + \frac{(z - l/2)}{l} \right) \tag{17}$$

with all the scalar coefficients $c_{uv} = 5$ and a 2% variation of the dielectric constant in all axial directions, giving $\Delta^{\%}_{\varepsilon'_{reff}} = 0.02$. The choice of f_{uv} in (15)-(17) assume the origin $(x, z = 0)$ is located at one of the corners of the dielectric filler.

C. SIMULATED SPECTRAL RESPONSES

The S-parameters for the dielectric-filled PEC-walled X-band PPWG are simulated, assuming waveguide operation

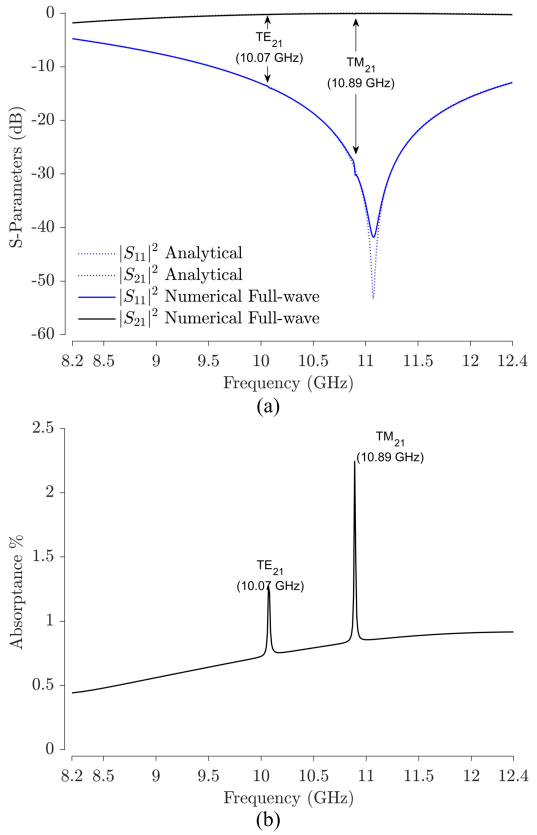

FIGURE 12. Simulated ABS-filled and PEC-walled X-band parallel-plate waveguide spectral responses: (a) $|S_{11}|^2$ and $|S_{21}|^2$; and (b) corresponding absorptance from full-wave simulations.

in the dominant TE_1 mode. The internal dimensions of the PPWG having wall separation distance $a = 22.860$ mm and dielectric-filled section length $l = 9.626$ mm; both corresponding to the previous X-band MPRWG dimensions [5]. For the numerical eigenmode solver only, the length of air-filled sections is now increased to $l_{air} = 17l$ (due to the extended evanescent fields of the TM_{11} mode) and terminated at both ends of the air-filled waveguide sections with 'second-order scattering boundary' surfaces. Moreover, the same X-band dielectric constant $\varepsilon'_{reff\,②} = 2.3284$ and loss tangent $tan\delta_{e②} = 19.148 \times 10^{-4}$ values were used for ABS [5]. The cut-off frequency for an air-filled section of this PPWG is $f_c^{TE1} = 6.5571$ GHz (identical to that for the dominant TE_{10} mode with the X-band MPRWG).

For an X-band PPWG operating in the dominant TE_1 mode, the simulated $|S_{11}|^2$ and $|S_{21}|^2$ frequency responses are given in Fig. 12(a). The solid lines in Fig. 12(a) correspond to numerical full-wave frequency-domain simulations, while dotted lines correspond to our analytical textbook S-parameter modeling (using modified versions of (A29) and (A30) in the Appendix); both clearly predict the driven Fabry-Pérot resonance at 11.07 GHz.

The mode indices m and p in $\tilde{f}_{mp}$ refer to the number of half-wavelength variations along the x- and z-directions, respectively, for either the E- or H-fields.

TABLE 3. Open-box mode resonance frequencies (and associated mode Q-factors) calculated using analytical and numerical eigenmode solvers and numerical frequency-domain simulator for the PEC-walled X-band parallel-plate waveguide shown in Fig. 11.

Open-box Mode		TE_{11}	TM_{11}	TE_{21}	TM_{21}
$\tilde{f}_{mp}$ [GHz] ($\lvert\tilde{f}_{mp}\rvert$) [$Q_u(f_{mp})$]	Analytical Eigenmode	5.6065+ *j*0.0036 (5.6065) [784]	6.1403+ *j*0.0013 (6.1403) [2305]	10.0732+ *j*0.0084 (10.0732) [600]	10.8927+ *j*0.0064 (10.8927) [845]
	Numerical Eigenmode	5.6063+ *j*0.0036 (5.6064) [784]	6.1402+ *j*0.0013 (6.1402) [2305]	10.0729+ *j*0.0084 (10.0729) [600]	10.8924+ *j*0.0064 (10.8924) [845]
	Numerical Full-wave	Below cut-off	Below cut-off	(10.07)	(10.89)

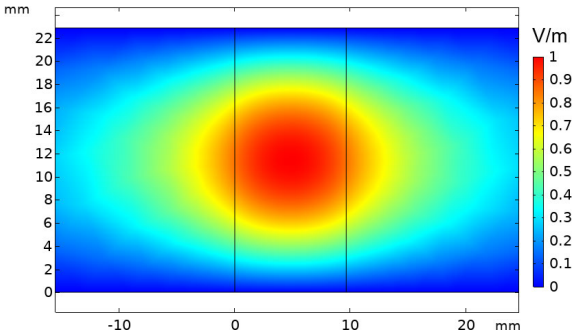

FIGURE 13. Numerically simulated E_y-field plot for the even TE_{11} Fabry-Pérot eigenmode below cut-off at $f_{11}^{TE} = 5.6064$ GHz.

The absorptance spectrum in Fig. 12(b) clearly shows parasitic TE_{21} and TM_{21} open-box mode resonances at $f_{21}^{TE} = 10.07$ and $f_{21}^{TM} = 10.89$ GHz, respectively; not clearly seen in Fig. 12(a).

The four lowest order parasitic Fabry-Pérot eigenmodes, along with the associated unloaded Q-factors, are predicted using our analytical and *COMSOL Multiphysics*® eigenmode solvers; the results are summarized in Table 3. From Table 3, it is clear that the first two parasitic Fabry-Pérot eigenmodes, TE_{11} at $f_{11}^{TE} = 5.6065$ GHz and TM_{11} at $f_{11}^{TM} = 6.1403$ GHz, are well below the $f_c^{TE1} = 6.5571$ GHz cut-off frequency for an air-filled PPWG. As shown in Table 3, these numerical full-wave frequency-domain predictions are within 0.01 GHz of those from both the analytical and numerical eigenmode solvers.

D. IDENTIFYING OPEN-BOX MODE RESONANCES FROM FIELD PLOTS

E-field plots, from the numerical eigenmode solver, for the X-band PPWG (with $l_{air} = 17l$) are shown in Figs. 13 to 16. It can be seen that for all the modes (TE_{11} and TM_{11} below cut-off and TE_{21} and TM_{21} above cut-off) the E-fields extend well outside the dielectric boundaries (represented by the two vertical black lines).

V. CIRCULAR WAVEGUIDES

A. BACKGROUND

Consider the PEC-walled CWG shown in Fig. 17.

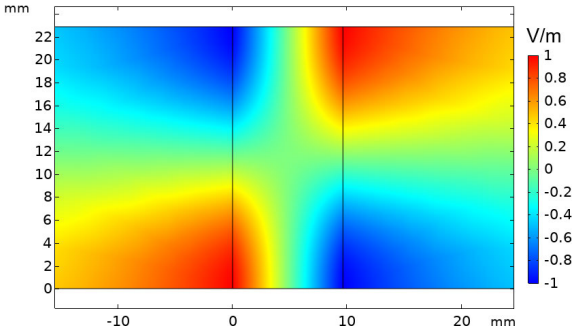

FIGURE 14. Numerically simulated E_x-field plot for the odd TM_{11} Fabry-Pérot eigenmode below cut-off at $f_{11}^{TM} = 6.1402$ GHz.

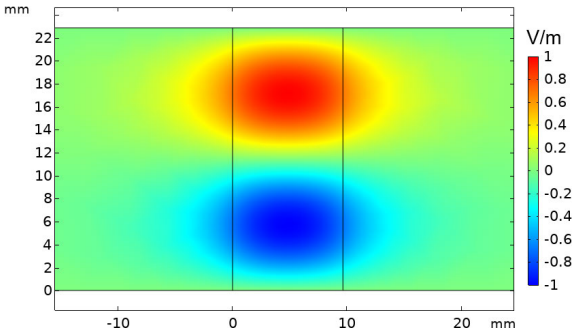

FIGURE 15. Numerically simulated E_y-field plot for the even TE_{21} Fabry-Pérot eigenmode at $f_{21}^{TE} = 10.0729$ GHz.

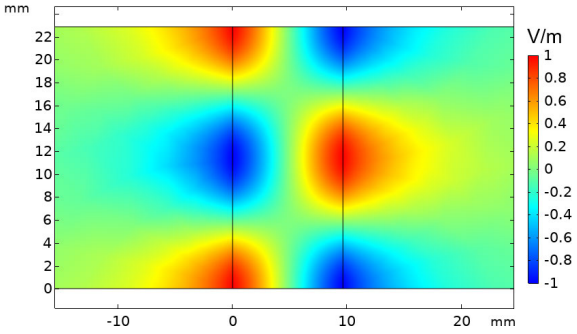

FIGURE 16. Numerically simulated E_x-field plot for the odd TM_{21} Fabry-Pérot eigenmode at $f_{21}^{TM} = 10.8924$ GHz.

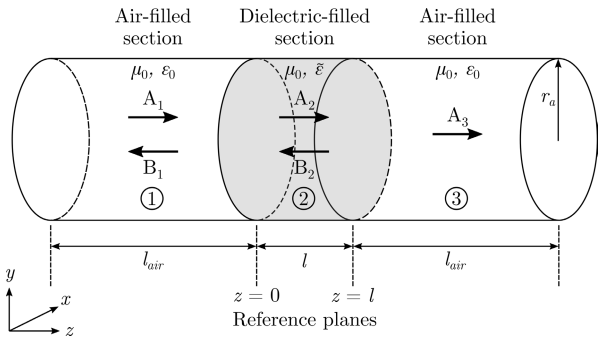

FIGURE 17. Illustration of an ideal dielectric-filled circular waveguide of radius r_a.

Subscripts m and n now refer to the number of half-wavelength radial (r) and circumferential (ϕ) variations, respectively, for either the E- or H-fields. The cut-off

TABLE 4. Values of p'_{mn} and p_{mn} for selected mn mode indices for the respective TE and TM modes in a PEC-walled circular waveguide. Table reproduced from Pozar [12].

n	TE			TM		
	p'_{1n}	p'_{2n}	p'_{3n}	p_{1n}	p_{2n}	p_{3n}
0	3.832	7.016	10.174	2.405	5.520	8.654
1	1.841	5.331	8.536	3.832	7.016	10.174
2	3.054	6.706	9.970	5.135	8.417	11.620

propagation constant for a CWG is [12],

$$\gamma_{cmn} = jk_{cmn} = \begin{cases} j\dfrac{p'_{mn}}{r_a} & \text{TE}_{\text{mn}} \text{ modes} \\ j\dfrac{p_{mn}}{r_a} & \text{TM}_{\text{mn}} \text{ modes} \end{cases} \tag{18}$$

Here, r_a is the internal radial distance from the axis of the circular waveguide to its PEC-walled boundary, p_{mn} is the m^{th} root of $J_n(x)$; such that $J_n(p_{mn}) = 0$, where $J_n(x)$ are the Bessel functions of the first kind. Similarly, p'_{mn} is the m^{th} root of $J'_n(p'_{mn}) = 0$, where the operator $J'_n(x)$ is the first derivative of $J_n(x)$. For both TE_{mn} and TM_{mn} propagating modes, the cut-off angular wavenumbers are $k_{cmn} = p'_{mn}/r_a$ and $k_{cmn} = p_{mn}/r_a$, respectively. The cut-off frequencies for the TE_{mn} and TM_{mn} propagating modes are then $f_{cmn} = k_c/2\pi\sqrt{\tilde{\mu}\tilde{\varepsilon}} = p'_{mn}/2\pi r_a\sqrt{\tilde{\mu}\tilde{\varepsilon}}$ and $f_{cmn} = k_c/2\pi\sqrt{\tilde{\mu}\tilde{\varepsilon}} = p_{mn}/2\pi r_a\sqrt{\tilde{\mu}\tilde{\varepsilon}}$, respectively. Selected values of p'_{mn} and p_{mn} are given in Table 4 (rounded to three decimal places).

The characteristic matrix equations for the TE_{mn} and TM_{mn} modes are exactly the same as (A12) and (A22). Moreover, the amplitude coefficients correspond to those in (A23)-(A26); the generalized coefficients ζ and ς correspond to (A27) and (A28), respectively; and the S-parameters S_{11} and S_{21} to (A29) and (A30), respectively. In a similar way to that undertaken for the MPRWG and PPWG, the associated even and odd modes can be obtained by numerically solving the analytical transcendental equations in (A35) and (A36) for the complex eigenfrequencies.

B. EXCITATION OF OPEN-BOX MODE RESONANCES WITH FREQUENCY-DOMAIN SIMULATOR

Following the approach outlined in Sections IIIB and IVB, for the excitation of open-box modes using an anisotropic dielectric constant tensor, a 3-D CWG was simulated using the *COMSOL Multiphysics*® full-wave frequency domain simulator.

Within *COMSOL Multiphysics*®, using (5), the signs for the terms in (6) are arbitrarily chosen for our simulated CWG, as follows,

$$\begin{aligned} f_{xx} &= f_{xy} = f_{yx} = f_{xz} = f_{zx} = f_{yz} = f_{zy} \\ &= \Delta^{\%}_{\varepsilon'_{reff}} \left(-\frac{x}{r_a} - \frac{y}{r_a} - \frac{(z - l/2)}{l} \right) \end{aligned} \tag{19}$$

$$f_{yy} = \Delta^{\%}_{\varepsilon'_{reff}} \left(-\frac{x}{r_a} + \frac{y}{r_a} + \frac{(z - l/2)}{l} \right) \tag{20}$$

$$f_{zz} = \Delta^{\%}_{\varepsilon'_{reff}} \left(\frac{x}{r_a} + \frac{y}{r_a} - \frac{(z - l/2)}{l} \right) \tag{21}$$

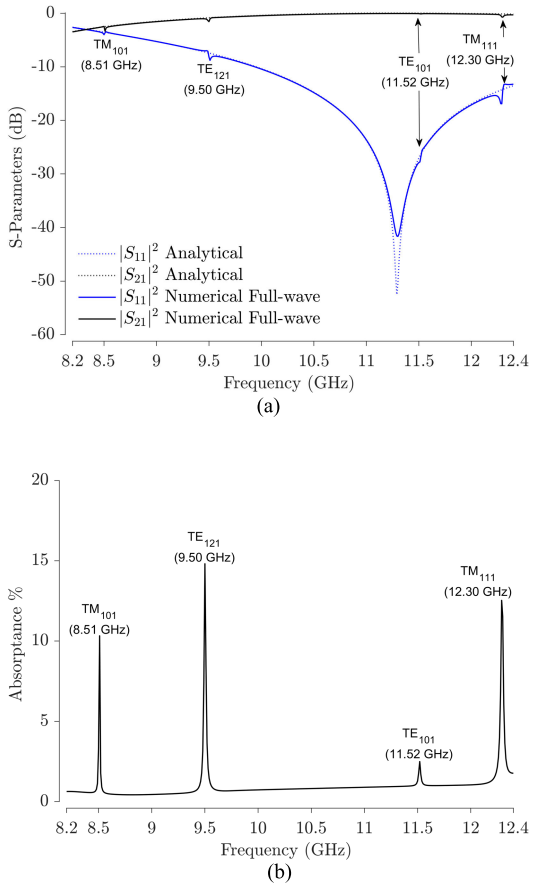

FIGURE 18. Simulated ABS-filled and PEC-walled X-band circular waveguide spectral responses: (a) $|S_{11}|^2$ and $|S_{21}|^2$; and (b) corresponding absorptance from full-wave simulations.

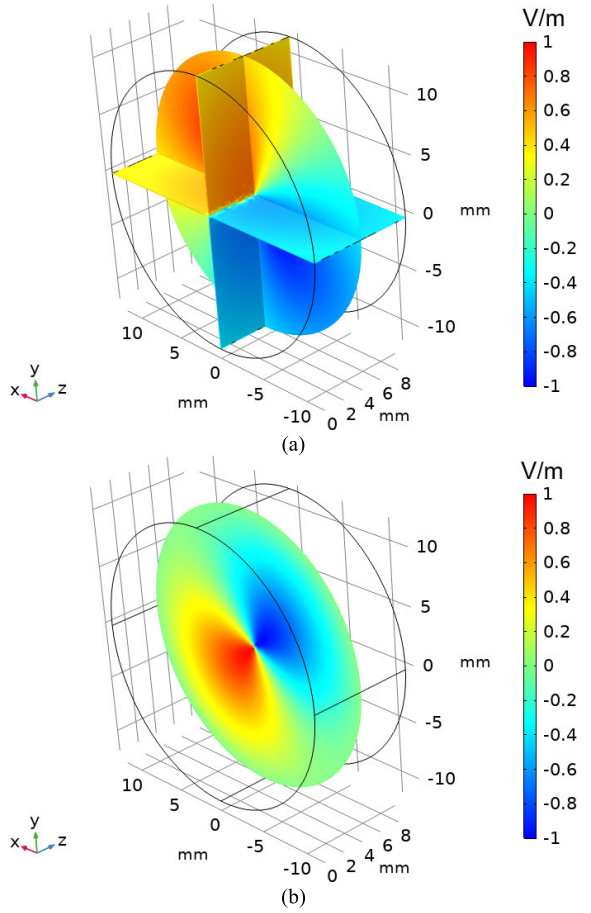

FIGURE 19. Numerically simulated field plots for the even TE_{111} Fabry-Pérot eigenmode below cut-off at $f_{111}^{TE} = 6.1921$ GHz: (a) E_r-field; (b) E_ϕ-field.

where all the scalars coefficients $c_{uv} = 5$ and a 2% variation of the dielectric constant in all axial directions, giving $\Delta^{\%}_{\varepsilon'_{reff}} = 0.02$. The choice of f_{uv} in (19)-(21) assumes that the z-axis lies in the middle of the circular waveguide with the origin $(x, y, z = 0)$ located at the center of the waveguide at one of the air-dielectric boundaries.

C. SIMULATED SPECTRAL RESPONSES

For our example, the circular waveguide is based on Electronic Industries Alliance (EIA) WC-94 standards, having an internal diameter of $2r_a = 23.825$ mm [13]; the dominant TE_{11} mode for an air-filled waveguide has a recommended frequency range of operation between 8.5 and 11.6 GHz within X-band. With an air-filled PEC circular waveguide, the lower-order cut-off frequencies f_c for the TE and TM modes are: $f_c^{TE11} = 1.84118 f_{co} = 7.375$ GHz (dominant mode); $f_c^{TM01} = 2.40483 f_{co} = 9.632$ GHz; $f_c^{TE21} = 3.05424 f_{co} = 12.186$ GHz; and $f_c^{TE01,TM11} = 3.83171 f_{co} = 15.347$ GHz, where $f_{co} = c/2\pi r_a = 4.005326$ GHz and $r_a = 11.9125$ mm is the internal radius for the WC-94 circular waveguide.

The S-parameters for the dielectric-filled PEC-walled X-band CWG are simulated, assuming waveguide operation in the dominant TE_{11} mode. The internal dielectric-filled section length $l = 9.626$ mm corresponds to that used previously for the X-band MPRWG [5] and PPWG. Moreover, the same X-band dielectric constant $\varepsilon'_{reff\,②} = 2.3284$ and loss tangent $tan\delta_{e②} = 19.148 \times 10^{-4}$ values are used for ABS [5].

For an X-band CWG operating in the dominant TE_{11} mode, the simulated $|S_{11}|^2$ and $|S_{21}|^2$ frequency responses are given in Fig. 18(a).

The solid lines in Fig. 18(a) correspond to numerical full-wave frequency-domain simulations, while dotted lines correspond to our analytical textbook S-parameter modeling (using (A29) and (A30) in the Appendix); both clearly predict the driven Fabry-Pérot resonance at 11.29 GHz.

The mode index p in $\tilde{f}_{mnp}$ refers to the number of half-wavelength variations along the z-direction, for either the E- or H-fields. The absorptance spectrum in Fig. 18(b) clearly shows parasitic TM_{101}, TE_{121}, TE_{101} and TM_{111} open-box mode resonances at $f_{101}^{TM} = 8.51$ GHz, $f_{121}^{TE} = 9.50$ GHz, $f_{101}^{TE} = 11.52$ GHz and $f_{111}^{TM} = 12.30$ GHz, respectively.

The open-box modes for the dielectric-filled CWG are simulated using analytical and numerical eigenmode solvers.

TABLE 5. Open-box mode resonance frequencies (and associated mode Q-factors) calculated using analytical and numerical eigenmode solvers for the PEC-walled X-band circular waveguide shown in Fig. 17.

Open-box Mode		TE_{111}	TM_{101}	TE_{121}	TE_{101}	TM_{111}
$\tilde{f}_{mnp}$ [GHz] ($\lvert\tilde{f}_{mnp}\rvert$) [$Q_u(f_{mnp})$]	Analytical Eigenmode	6.1917+ *j*0.0042 (6.1917) [736]	8.5110+ *j*0.0035 (8.5110) [1214]	9.4930+ *j*0.0078 (9.4930) [611]	11.5292+ *j*0.0099 (11.5292) [581]	12.3315+ *j*0.0083 (12.3315) [742]
	Numerical Eigenmode	6.1921+ *j*0.0042 (6.1921) [736]	8.5101+ *j*0.0035 (8.5101) [1214]	9.4936+ *j*0.0078 (9.4936) [611]	11.5285+ *j*0.0099 (11.5285) [581]	12.3299+ *j*0.0083 (12.3299) [742]
	Numerical Full-wave	Below cut-off	(8.51)	(9.50)	(11.52)	(12.30)

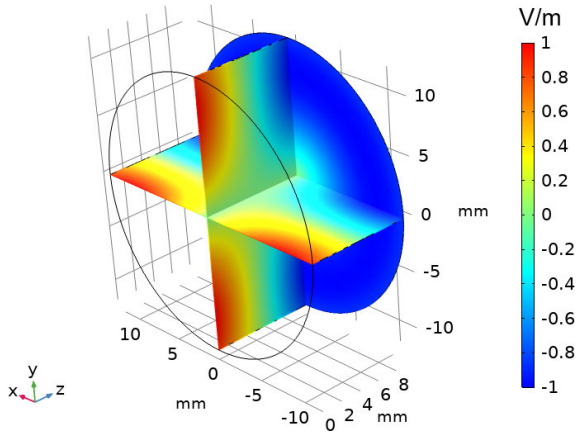

FIGURE 20. Numerically simulated E_r-field plot for the odd TM_{101} Fabry-Pérot eigenmode at $f_{101}^{TM} = 8.5101$ GHz.

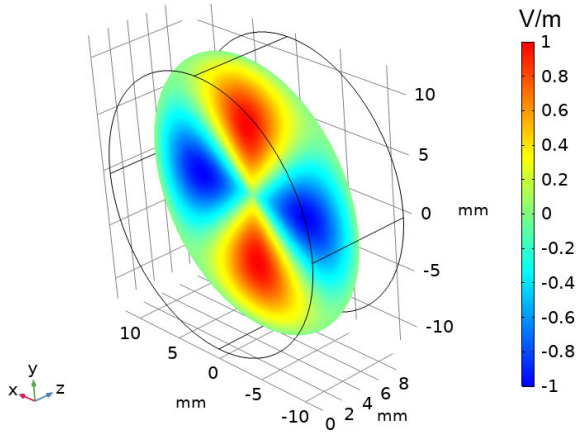

FIGURE 21. Numerically simulated E_ϕ-field plot for the even TE_{121} Fabry-Pérot eigenmode at $f_{121}^{TE} = 9.4936$ GHz.

The resulting eigenfrequencies are given in Table 5. Here, the TE_{111} open-box mode at $f_{111}^{TE} = 6.1917$ GHz is below the $f_c^{TE11} = 7.375$ GHz cut-off frequency and not seen in the spectral responses. As shown in Table 5, these numerical full-wave frequency-domain predictions are within 0.03 GHz of those from our analytical and numerical eigenmode methods.

D. IDENTIFYING OPEN-BOX MODE RESONANCES FROM FIELD PLOTS

E-field plots, from the numerical eigenmode solver, for the X-band CWG are shown in Figs. 19 to 23. Here, isometric views are needed with cut-planes in order to uniquely identify the modes. For example, the TE_{111} mode in Fig. 19(b) appears identical to the TM_{111} mode in Fig. 23; the two different

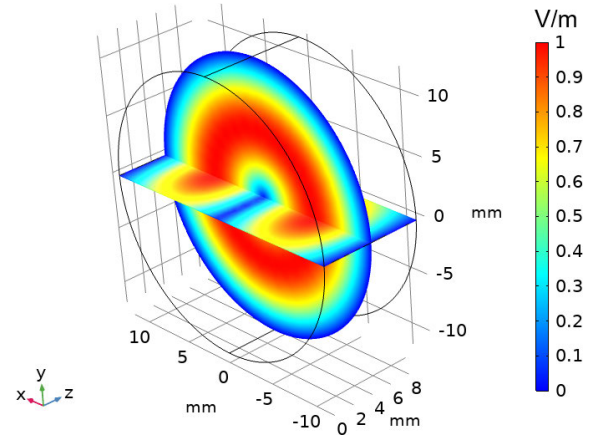

FIGURE 22. Numerically simulated E_ϕ-field plot for the even TE_{101} Fabry-Pérot eigenmode at $f_{101}^{TE} = 11.5285$ GHz.

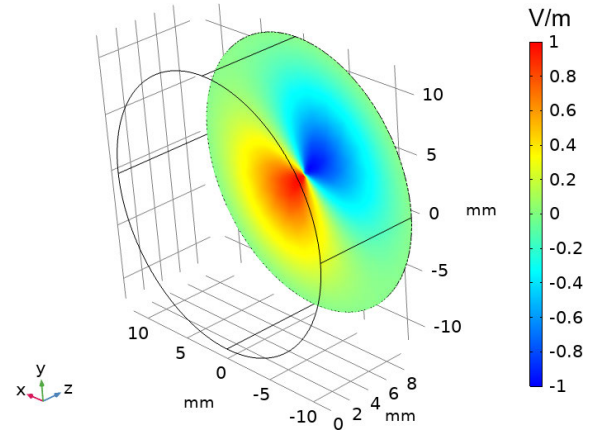

FIGURE 23. Numerically simulated E_ϕ-field plot for the odd TM_{111} Fabry-Pérot eigenmode at $f_{111}^{TM} = 12.3299$ GHz.

modes can be differentiated by knowing the longitudinal position of their cuts (located at center and with quarter-wavelength offset, respectively).

VI. DISCUSSION AND CONCLUSION

Open-box mode resonances have been found in a survey of microwave measurements of 3-D printed cuboid samples within MPRWGs. These parasitic Fabry-Pérot eigenmodes were either ignored or not rigorously investigated. These parasitic resonances can exhibit very high Q-factors (shown here to exceed 2,300 with a PEC-walled X-band PPWG), which may offer the potential for future exploitation.

The authors of this paper previously studied open-box mode resonances within dielectric-filled MPRWGs, using both analytical and numerical eigenmode solvers. This preliminary work has now been extended in this paper, to cover three conventional types of dielectric-filled metal waveguides (MPRWGs, PPWGs and CWGs).

While previously speculating that open-box mode resonances can be excited within inhomogeneous and/or anisotropic media (3-D printed cuboids in this case), we have now proven that parasitic Fabry-Pérot eigenmodes exist with inhomogeneous and anisotropic dielectrics.

Complex eigenfrequencies for dielectric-filled waveguide structures were obtained by numerically solving analytical transcendental equations for the lowest-order even and odd eigenmodes. These results were compared against those obtained from the numerical *COMSOL Multiphysics*® eigenmode solver, showing excellent agreement. Moreover, from either the E- or H-field patterns, we have accurately identified the type of open-box modes, below and above the lowest cut-off frequencies associated with the corresponding air-filled waveguides.

Furthermore, we have demonstrated a new technique for studying open-box mode resonances that employs numerical full-wave frequency-domain simulations. Here, the inhomogeneous and anisotropic nature of the woodpile-like dielectric structure (physical realm) is represented by an anisotropic dielectric constant tensor (simulation realm).

The common scalar coefficient representing the level of coupling between different field components due to anisotropy was chosen to be $c_{uv} = 1$ for the MPRWG and 5 for both PPWG and CWG. With the variation of the dielectric constant in all axial directions, a fixed value of $\Delta^{\%}_{\varepsilon'_{reff}} = 0.02$ was adopted for all the waveguide structures. Both control parameters are perturbed just enough (with their lowest values) to reveal the presence of the parasitic open-box modes in the S-parameters, while being validated by practical measurements (in the case of the MPRWG).

The *COMSOL Multiphysics*® frequency-domain simulations accurately predicted the spectral location of the undamped resonance frequencies for all in-band parasitic open-box modes; to within 0.03 GHz of those obtained from the analytical and numerical eigenmode solvers for all waveguide structures (and within approximately 0.1 GHz and 0.2 GHz when compared to measurements at X- and Ku-bands, respectively, for the metal-pipe rectangular waveguide). Note that, additional simulations of a PPWG having a dielectric-filler that is inhomogeneous and isotropic does not excite all the open-box modes.

This paper provides the foundation for accurately modeling the parasitic resonances associated with inhomogeneity and anisotropy in 3-D printed microwave components; not just the metal-walled waveguide structures considered here, but the methodology could also be extended to generic 3-D printed dielectric waveguides and substrate-based transmission lines (e.g., printed microstrip, stripline and suspended microstrip [14]). In addition, our work can be applied to engineered metamaterials within waveguides and transmission lines. For example, periodically-loaded dielectric slabs could be inserted within a metal-pipe waveguide, such that the lowest order open-box mode below the air-filled cut-off frequency can result in wave propagation via evanescent mode coupling between slabs.

APPENDIX

With reference to Figs. 1, 11 and 17, under steady-state sinusoidal excitation, there will be forward and backward travelling waves, with *A*s representing complex amplitude coefficients for the forward travelling waves and *B*s representing the backward travelling waves. There are no reflected waves within Section ③ of the waveguide structure. It is assumed that Sections ① and ③ have the same material parameters.

With the MPRWG, for the TE$_{mn}$ mode the electric (E-)field and magnetic (H-)field components within the three waveguide sections are [5],

$$E_{y①} = \frac{\omega\tilde{\mu}_{①}\gamma_{cm0}}{\gamma_{cmn}^2}\left(A_{mn①}e^{-\gamma_{mn①}z} + B_{mn①}e^{\gamma_{mn①}z}\right) \times \sin(k_{cm0}x)\cos(k_{c0n}y) \tag{A1}$$

$$H_{x①} = -j\frac{\gamma_{mn①}\gamma_{cm0}}{\gamma_{cmn}^2}\left(A_{mn①}e^{-\gamma_{mn①}z} - B_{mn①}e^{\gamma_{mn①}z}\right) \times \sin(k_{cm0}x)\cos(k_{c0n}y) \tag{A2}$$

$$H_{z①} = \left(A_{mn①}e^{-\gamma_{mn①}z} - B_{mn①}e^{\gamma_{mn①}z}\right) \times \cos(k_{cm0}x)\cos(k_{c0n}y) \tag{A3}$$

$$E_{y②} = \frac{\omega\tilde{\mu}_{②}\gamma_{cm0}}{\gamma_{cmn}^2}\left(A_{mn②}e^{-\gamma_{mn②}z} + B_{mn②}e^{\gamma_{mn②}z}\right) \times \sin(k_{cm0}x)\cos(k_{c0n}y) \tag{A4}$$

$$H_{x②} = -j\frac{\gamma_{mn②}\gamma_{cm0}}{\gamma_{cmn}^2}\left(A_{mn②}e^{-\gamma_{mn②}z} - B_{mn②}e^{\gamma_{mn②}z}\right) \times \sin(k_{cm0}x)\cos(k_{c0n}y) \tag{A5}$$

$$H_{z②} = \left(A_{mn②}e^{-\gamma_{mn②}z} - B_{mn②}e^{\gamma_{mn②}z}\right) \times \cos(k_{cm0}x)\cos(k_{c0n}y) \tag{A6}$$

$$E_{y③} = \frac{\omega\tilde{\mu}_{①}\gamma_{cm0}}{\gamma_{cmn}^2}A_{mn③}e^{-\gamma_{mn①}(z-l)} \times \sin(k_{cm0}x)\cos(k_{c0n}y) \tag{A7}$$

$$H_{x③} = -j\frac{\gamma_{mn①}\gamma_{cm0}}{\gamma_{cmn}^2}A_{mn③}e^{-\gamma_{mn①}(z-l)} \times \sin(k_{cm0}x)\cos(k_{c0n}y) \tag{A8}$$

$$H_{z③} = A_{mn③}e^{-\gamma_{mn①}(z-l)}\cos(k_{cm0}x)\cos(k_{c0n}y) \tag{A9}$$

where the textbook cut-off propagation constant is,

$$\gamma_{cmn} = jk_{cmn} = j\sqrt{\left(\frac{m\pi}{a}\right)^2 + \left(\frac{n\pi}{b}\right)^2} \tag{A10}$$

and,

$$k_{cm0} = \frac{m\pi}{a} \text{ and } k_{c0n} = \frac{n\pi}{b} \tag{A11}$$

Here, m and n correspond to the mode numbers in the horizontal x- and vertical y-directions in the transverse plane, respectively; $\gamma_{mn①}$ and $\gamma_{mn②}$ are the generalized propagation constants for the TE$_{mn}$ mode within Sections ①, ③, and Section ②, respectively. With respect to Fig. 1, $\gamma_{mn①} \rightarrow \gamma_{10}^{air}$ and $\gamma_{mn②} \rightarrow \gamma_{10}$ are the propagation constants for the TE$_{10}$ mode within the air-filled (Sections ①, ③) and dielectric-filled (Section ②) waveguide sections, respectively. All calculations assume a waveguide with PEC walls. The reference plane for fields with coefficient $A_{mn③}$ is $z = l$, as indicated by the $z - l$ shift in the term $A_{mn③}e^{-\gamma_{mn①}(z-l)}$. The reference plane for all other coefficients is $z = 0$.

By applying TE mode continuity boundary conditions for the MPRWG (and PPWG): $E_{y①}(z=0)=E_{y②}(z=0)$, $E_{y②}(z=l)=E_{y③}(z=l)$, $H_{x①}(z=0)=H_{x②}(z=0)$, $H_{x②}(z=l)=H_{x③}(z=l)$, and after some algebraic manipulations, the following characteristic matrix equation is obtained for TE_{mn} modes,

$$\begin{bmatrix} \tilde{\mu}_{①} & \tilde{\mu}_{①} & -\tilde{\mu}_{②} & -\tilde{\mu}_{②} & 0 \\ \gamma_{mn①} & -\gamma_{mn①} & -\gamma_{mn②} & \gamma_{mn②} & 0 \\ 0 & 0 & \tilde{\mu}_{②}e^{-\gamma_{mn②}l} & \tilde{\mu}_{②}e^{\gamma_{mn②}l} & -\tilde{\mu}_{①} \\ 0 & 0 & \gamma_{mn②}e^{-\gamma_{mn②}l} & -\gamma_{mn②}e^{\gamma_{mn②}l} & -\gamma_{mn①} \end{bmatrix} \times \begin{bmatrix} A_{mn①} \\ B_{mn①} \\ A_{mn②} \\ B_{mn②} \\ A_{mn③} \end{bmatrix} = \begin{bmatrix} 0 \\ 0 \\ 0 \\ 0 \end{bmatrix} \tag{A12}$$

For the TM_{mn} mode, the E-field and H-field components within the three waveguide sections are [5],

$$E_{x①} = -j\frac{\gamma_{mn①}\gamma_{cm0}}{\gamma_{cmn}^2}\left(A_{mn①}e^{-\gamma_{mn①}z} + B_{mn①}e^{\gamma_{mn①}z}\right) \times \cos(k_{cm0}x)\sin(k_{c0n}y) \tag{A13}$$

$$H_{y①} = \frac{\omega\tilde{\varepsilon}_{①}\gamma_{cm0}}{\gamma_{cmn}^2}\left(A_{mn①}e^{-\gamma_{mn①}z} - B_{mn①}e^{\gamma_{mn①}z}\right) \times \cos(k_{cm0}x)\sin(k_{c0n}y) \tag{A14}$$

$$E_{z①} = \left(A_{mn①}e^{-\gamma_{mn①}z} + B_{mn①}e^{\gamma_{mn①}z}\right) \times \sin(k_{cm0}x)\sin(k_{c0n}y) \tag{A15}$$

$$E_{x②} = -j\frac{\gamma_{mn②}\gamma_{cm0}}{\gamma_{cmn}^2}\left(A_{mn②}e^{-\gamma_{mn②}z} + B_{mn②}e^{\gamma_{mn①}z}\right) \times \cos(k_{cm0}x)\sin(k_{c0n}y) \tag{A16}$$

$$H_{y②} = \frac{\omega\tilde{\varepsilon}_{②}\gamma_{cm0}}{\gamma_{cmn}^2}\left(A_{mn②}e^{-\gamma_{mn①}z} - B_{mn②}e^{\gamma_{mn①}z}\right) \times \cos(k_{cm0}x)\sin(k_{c0n}y) \tag{A17}$$

$$E_{z②} = \left(A_{mn②}e^{-\gamma_{mn②}z} + B_{mn②}e^{\gamma_{mn①}z}\right) \times \sin(k_{cm0}x)\sin(k_{c0n}y) \tag{A18}$$

$$E_{x③} = -j\frac{\gamma_{mn③}\gamma_{cm0}}{\gamma_{cmn}^2}A_{mn③}e^{-\gamma_{mn①}(z-l)} \times \cos(k_{cm0}x)\sin(k_{c0n}y) \tag{A19}$$

$$H_{y③} = \frac{\omega\tilde{\varepsilon}_{③}\gamma_{cm0}}{\gamma_{cmn}^2}A_{mn③}e^{-\gamma_{mn①}(z-l)} \times \cos(k_{cm0}x)\sin(k_{c0n}y) \tag{A20}$$

$$E_{z③} = A_{mn③}e^{-\gamma_{mn①}(z-l)}\sin(k_{cm0}x)\sin(k_{c0n}y) \tag{A21}$$

By applying TM mode continuity boundary conditions for the MPRWG (and PPWG): $E_{x①}(z=0)=E_{x②}(z=0)$, $E_{x②}(z=l)=E_{x③}(z=l)$, $H_{y①}(z=0)=H_{y②}(z=0)$, $H_{y②}(z=l)=H_{y③}(z=l)$, and after some algebraic manipulations, the following characteristic matrix equation is obtained for TM_{mn} modes,

$$\begin{bmatrix} \gamma_{mn①} & \gamma_{mn①} & -\gamma_{mn②} & -\gamma_{mn②} & 0 \\ \tilde{\varepsilon}_{①} & -\tilde{\varepsilon}_{①} & -\tilde{\varepsilon}_{②} & \tilde{\varepsilon}_{②} & 0 \\ 0 & 0 & \gamma_{mn②}e^{-\gamma_{mn②}l} & \gamma_{mn②}e^{\gamma_{mn②}l} & -\gamma_{mn①} \\ 0 & 0 & \tilde{\varepsilon}_{②}e^{-\gamma_{mn②}l} & -\tilde{\varepsilon}_{②}e^{\gamma_{mn②}l} & -\tilde{\varepsilon}_{①} \end{bmatrix} \times \begin{bmatrix} A_{mn①} \\ B_{mn①} \\ A_{mn②} \\ B_{mn②} \\ B_{mn③} \end{bmatrix} = \begin{bmatrix} 0 \\ 0 \\ 0 \\ 0 \end{bmatrix} \tag{A22}$$

While the MPRWG has been used to derive (A12) and (A22) for the TE and TM modes, respectively, they are generic and can also be used for the PPWG and CWG by the appropriate substitution of the cut-off propagation constant in (2).

For convenience, the waveguides in Figs. 1, 11 and 17 are excited by setting $A_{mn①}$ to unity and the rest of the amplitude coefficients can then be obtained from (A12) or (A22),

$$B_{mn①} = \frac{\left(1-e^{-2\gamma_{mn②}l}\right)(1-\zeta)(1+\zeta)}{(1+\zeta)^2 - e^{-2\gamma_{mn②}l}(1-\zeta)^2} \tag{A23}$$

$$A_{mn②} = \frac{-2\varsigma(1+\zeta)}{(1+\zeta)^2 - e^{-2\gamma_{mn②}l}(1-\zeta)^2} \tag{A24}$$

$$B_{mn②} = \frac{-2\varsigma e^{-2\gamma_{mn②}l}(1-\zeta)}{(1+\zeta)^2 - e^{-2\gamma_{mn②}l}(1-\zeta)^2} \tag{A25}$$

$$A_{mn③} = \frac{4\zeta e^{-\gamma_{mn②}l}}{(1+\zeta)^2 - e^{-2\gamma_{mn②}l}(1-\zeta)^2} \tag{A26}$$

with generalized coefficients,

$$\zeta = \begin{cases} \dfrac{\gamma_{mn②}\tilde{\mu}_{①}}{\gamma_{mn①}\tilde{\mu}_{②}} & \mathrm{TE}_{mn}\ \text{modes} \\ \dfrac{\gamma_{mn①}\tilde{\varepsilon}_{②}}{\gamma_{mn②}\tilde{\varepsilon}_{①}} & \mathrm{TM}_{mn}\ \text{modes} \end{cases} \tag{A27}$$

and,

$$\varsigma = \begin{cases} \dfrac{\tilde{\mu}_{①}}{\tilde{\mu}_{②}} & \mathrm{TE}_{mn}\ \text{modes} \\ \dfrac{\gamma_{mn①}}{\gamma_{mn②}} & \mathrm{TM}_{mn}\ \text{modes} \end{cases} \tag{A28}$$

S-parameters can now be defined as,

$$S_{11} \equiv \left.\frac{B_{mn①}}{A_{mn①}}\right|_{B_{mn③}=0} \rightarrow B_{mn①}\ \text{with}\ A_{mn①}=1 \tag{A29}$$

and,

$$S_{21} \equiv \left.\frac{A_{mn③}}{A_{mn①}}\right|_{B_{mn③}=0} \rightarrow A_{mn③} \text{ with } A_{mn①} = 1 \quad \text{(A30)}$$

Setting $A_{mn①} = 1$ corresponds to a driven excitation, while $A_{mn①} = 0$ indicates undriven excitation. With the former, with no waveguide wall or dielectric losses, at the Fabry-Pérot resonance frequency, there is a return loss zero with $B_{mn①} = 0$ and $A_{mn③} = 1$. With the latter, the complex eigenfrequency response can be obtained (and as long as $B_{mn①} \neq 0$) by setting the denominator of $B_{mn①}$ to zero in (A23).

With a PEC-walled waveguide, the propagation constant for an unbound dielectric in (2) is given as [5],

$$\gamma_{ud}^2 = \gamma_{mn}^2 + \gamma_{cmn}^2 = -\omega^2 \tilde{\mu}\tilde{\varepsilon} \quad \text{(A31)}$$

With the scenario depicted in Fig. 1, $\tilde{\mu}_{①,③} = \mu_0\tilde{\mu}_{r①,③} \rightarrow \mu_0$, $\tilde{\mu}_{②} = \mu_0\tilde{\mu}_{r②} \rightarrow \mu_0\mu_r'$, $\tilde{\varepsilon}_{①,③} = \varepsilon_0\tilde{\varepsilon}_{reff①,③} \rightarrow \varepsilon_0$ and $\tilde{\varepsilon}_{②} = \varepsilon_0\tilde{\varepsilon}_{reff②} \rightarrow \varepsilon_0\tilde{\varepsilon}_{reff}$. Therefore, the respective guided-wave propagation constants for Sections ①,③ and Section ② are [5],

$$\gamma_{mn①,③} = \sqrt{k_{cmn}^2 - \omega^2\tilde{\mu}_{①,③}\tilde{\varepsilon}_{①,③}} \rightarrow \sqrt{k_{cmn}^2 - \omega^2\mu_0\varepsilon_0} \quad \text{(A32)}$$

$$\gamma_{mn②} = \sqrt{k_{cmn}^2 - \omega^2\tilde{\mu}_{②}\tilde{\varepsilon}_{②}} \rightarrow \sqrt{k_{cmn}^2 - \omega^2\mu_0\mu_r'\varepsilon_0\tilde{\varepsilon}_{reff}} \quad \text{(A33)}$$

As mentioned earlier, the associated complex eigenfrequencies are defined by the poles of $B_{mn①}$, in (A23), by setting its denominator to zero (i.e., to extract its undriven natural modes without any external steady-state sinusoidal excitation, so that $A_{mn①} = 0$) [5],

$$(1+\zeta)^2 - e^{-2\gamma_{mn②}l}(1-\zeta)^2 = 0 \quad \text{(A34)}$$

An infinite number of solutions emerge from (A34), which are either designated as even or odd modes – depending on the corresponding longitudinal symmetry of the electric field. These even and odd modes can be obtained by solving the following transcendental equations for complex eigenfrequencies [5],

$$(1+\zeta) + e^{-\gamma_{mn②}l}(1-\zeta) = 0 \quad \text{Even modes} \quad \text{(A35)}$$

$$(1+\zeta) - e^{-\gamma_{mn②}l}(1-\zeta) = 0 \quad \text{Odd modes} \quad \text{(A36)}$$

The roots of (A35) and (A36) can be numerically solved to obtain the complex angular eigenfrequencies $\tilde{\omega}_{mnp} = \omega_{mnp}' + j\omega_{mnp}''$ for the even and odd open-box modes, respectively; the undamped (or driven) resonance frequencies, normally associated with frequency-domain simulations, is $f_{mnp} = |\tilde{\omega}_{mnp}|/2\pi$. The mode indices m, n and p in $\tilde{f}_{mnp}$ refer to the number of half-wavelength variations in the transverse plane and longitudinal direction, respectively, for either the E- or H-fields. Here, the multiple solutions from (A35) and (A36) correspond to different mode index values of p.

Equations (35) for even modes and (36) for odd modes can be decomposed to give TE and TM solutions. For example, the following transcendental equations are obtained for the TE$_{mn}$ modes,

$$\tilde{\mu}_①\gamma_{mn②} - \tilde{\mu}_②\gamma_{mn①}\coth\left(\frac{\gamma_{mn②}l}{2}\right) = 0 \quad \text{Even modes} \quad \text{(A37)}$$

$$\tilde{\mu}_①\gamma_{mn②} - \tilde{\mu}_②\gamma_{mn①}\tanh\left(\frac{\gamma_{mn②}l}{2}\right) = 0 \quad \text{Odd modes} \quad \text{(A38)}$$

These expressions can be further simplified by setting $\tilde{\mu}_① = \tilde{\mu}_②/\mu_r' = \mu_0$ to obtain,

$$\mu_r'\gamma_{mn①} - \gamma_{mn②}\tanh\left(\frac{\gamma_{mn②}l}{2}\right) = 0 \quad \text{Even modes} \quad \text{(A39)}$$

$$\gamma_{mn②} - \mu_r'\gamma_{mn①}\tanh\left(\frac{\gamma_{mn②}l}{2}\right) = 0 \quad \text{Odd modes} \quad \text{(A40)}$$

A similar approach can be used to derive the following simplified equations for the TM$_{mnp}$ open-box modes, with $\tilde{\varepsilon}_① = \tilde{\varepsilon}_②/\tilde{\varepsilon}_{reff} = \varepsilon_0$ [5],

$$\gamma_{mn②} - \tilde{\varepsilon}_{reff}\gamma_{mn①}\tanh\left(\frac{\gamma_{mn②}l}{2}\right) = 0 \quad \text{Even modes} \quad \text{(A41)}$$

$$\tilde{\varepsilon}_{reff}\gamma_{mn①} - \gamma_{mn②}\tanh\left(\frac{\gamma_{mn②}l}{2}\right) = 0 \quad \text{Odd modes} \quad \text{(A42)}$$

ACKNOWLEDGMENT

The authors would like to thank S. Papantonis at Computer Simulation Technology (CST) for his useful discussions on field simulations. In addition, they wish to thank N. Ridler at the National Physical Laboratory, U.K., for facilitating the original measurements in [5] and [6].

REFERENCES

[1] W. J. Otter and S. Lucyszyn, "3-D printing of microwave components for 21st century applications," in *IEEE MTT-S Int. Microw. Symp. Dig.*, Chengdu, China, Jul. 2016, pp. 1–3.

[2] M. D'Auria, W. J. Otter, J. Hazell, B. T. W. Gillatt, C. Long-Collins, N. M. Ridler, and S. Lucyszyn, "3-D printed metal-pipe rectangular waveguides," *IEEE Trans. Compon., Packag., Manuf. Technol.*, vol. 5, no. 9, pp. 1339–1349, Sep. 2015.

[3] B. T. W. Gillatt, M. D'Auria, W. J. Otter, N. M. Ridler, and S. Lucyszyn, "3-D printed variable phase shifter," *IEEE Microw. Wireless Compon. Lett.*, vol. 26, no. 10, pp. 822–824, Oct. 2016.

[4] S.-H. Shin, D. F. Alyasiri, M. D'Auria, W. J. Otter, C. W. Myant, D. Stokes, Z. Tian, N. M. Ridler, and S. Lucyszyn, "Polymer-based 3-D printed Ku-band steerable phased-array antenna subsystem," *IEEE Access*, vol. 7, pp. 106662–106673, 2019.

[5] J. Sun, A. Dawood, W. J. Otter, N. M. Ridler, and S. Lucyszyn, "Microwave characterization of low-loss FDM 3-D printed ABS with dielectric-filled metal-pipe rectangular waveguide spectroscopy," *IEEE Access*, vol. 7, pp. 95455–95486, 2019.

[6] E. Márquez-Segura, S.-H. Shin, A. Dawood, N. M. Ridler, and S. Lucyszyn, "Microwave characterization of conductive PLA and its application to a 12 to 18 GHz 3-D printed rotary vane attenuator," *IEEE Access*, vol. 9, pp. 84327–84343, 2021.
[7] A. G. Knisely, "Biaxial anisotropic material development and characterization using rectangular to square waveguide," M.S. thesis, Dept. Elect. Comput. Eng., Air Force Inst. Technol., Wright-Patterson Air Force Base, OH, USA, Tech. Rep. AFIT-ENG-MS-15-M-055, Mar. 2015.
[8] D. V. Isakov, Q. Lei, F. Castles, C. J. Stevens, C. R. M. Grovenor, and P. S. Grant, "3D printed anisotropic dielectric composite with meta-material features," *Mater. Des.*, vol. 93, pp. 423–430, Mar. 2016.
[9] C. Yang, J. Wang, and F. Feng, "An improved technique for low-loss material complex permittivity and permeability determination from transmission-only measurements," *Frequenz*, vol. 74, nos. 11–12, pp. 435–439, Nov. 2020.
[10] *COMSOL RF Module*. Accessed: Jun. 29, 2021. [Online]. Available: https://uk.comsol.com/rf-module
[11] S. Papantonis and S. Lucyszyn, "Lossy spherical cavity resonators for stress-testing arbitrary 3D eigenmode solvers," *Prog. Electromagn. Res.*, vol. 151, pp. 151–167, 2015.
[12] D. M. Pozar, "Transmission lines and waveguides," in *Microwave Engineering*, 3rd ed. New York, NY, USA: Wiley, 2005, pp. 102–110.
[13] H.-U. Nickel. (Sep. 2020). *Cross Reference for Hollow Metallic Waveguides*. Accessed: Sep. 24, 2021. [Online]. Available: https://www.spinner-group.com/images/download/technical_documents/SPINNER_TD00036.pdf
[14] P. I. Deffenbaugh, T. M. Weller, and K. H. Church, "Fabrication and microwave characterization of 3-D printed transmission lines," *IEEE Microw. Wireless Compon. Lett.*, vol. 25, no. 12, pp. 823–825, Dec. 2015.

ATTIQUE DAWOOD received the M.S. degree in electrical engineering from the National University of Computer and Emerging Sciences, Islamabad, Pakistan, in 2012, and the Ph.D. degree from Imperial College London, London, U.K., in 2020. His current research interest includes electromagnetic modeling of passive structures from microwaves to terahertz frequencies.

STEPAN LUCYSZYN (Fellow, IEEE) received the Ph.D. degree in electronic engineering from King's College London, University of London, London, U.K., in 1992, and the D.Sc. (higher doctorate) degree in millimeter-wave and terahertz electronics from Imperial College London, London, U.K., in 2010.

He is currently a Professor of millimeter-wave systems at Imperial College London. He has coauthored well over 200 papers and 12 book chapters in applied physics and electronic engineering. He was made a fellow of the Institution of Electrical Engineers, U.K., and the Institute of Physics, U.K., in 2005. In 2008, he became a fellow of the Electromagnetics Academy, USA. He was appointed as an IEEE Distinguished Microwave Lecturer, from 2010 to 2013. He co-founded the Imperial College London spin-out company Drayson Wireless Ltd., in 2014.